

Mixture of Inverse Gaussians for Hemodynamic Transport (MIGHT) in Vascular Networks

Timo Jakumeit¹, Bastian Heinlein^{1,2}, Leonie Richter¹, Sebastian Lotter¹, Robert Schober¹, and Maximilian Schäfer¹

¹ Friedrich-Alexander-Universität Erlangen-Nürnberg, Erlangen, Germany

² Technical University of Darmstadt, Darmstadt, Germany

Abstract—Synthetic molecular communication (MC) in the cardiovascular system (CVS) is a key enabler for many envisioned medical applications in the human body, such as targeted drug delivery, early cancer detection, and continuous health monitoring. The design of MC systems for such applications requires suitable models for the signaling molecule propagation through complex vessel networks (VNs). Existing theoretical models offer limited analytical tractability and lack closed-form solutions, making the analysis of large-scale VNs either infeasible or not insightful. To overcome these limitations, in this paper, we propose a novel closed-form physical model, termed *MIGHT*, for advection-diffusion-driven transport of signaling molecules through complex VNs. The model represents the received molecule flux as a weighted sum of inverse Gaussian (IG) distributions, parameterized by physical properties of the network. The proposed model is validated by comparison with an existing convolution-based model and finite-element simulations. Further, we show that the model can be applied for the reduction of large VNs to simplified representations preserving the essential transport dynamics and for estimating representative VN based on received signals from unknown VNs.

Index Terms—Molecular communication, vascular network, inverse Gaussian distribution, advection-diffusion

I. INTRODUCTION

Located at the crossroads of communications engineering and life sciences, synthetic molecular communication (MC) investigates the exchange of information between bio-chemical devices based on signaling molecules and can provide critical insights and tools for the realization of emerging medical applications, such as the Internet of Bio-Nano Things (IoBNT), early cancer detection and localization, and targeted drug delivery [1]–[3]. In medical MC applications, the cardiovascular system (CVS) is the main envisioned application domain due to its pervasiveness in the human body and significance for vital physiological processes. In order to realize MC applications in the CVS, it is crucial to derive suitable channel models characterizing molecule propagation in the complex vessel networks (VNs) within the CVS [4]. While early works in MC mainly modeled propagation within isolated vessels, it has become clear that a comprehensive understanding of complex VNs is essential. Often, the topology of the VN influences signal dynamics more strongly than fine-grained physical processes within individual vessels [5]. As such, physically accurate and insightful *network-level* models are indispensable.

Especially the derivation of analytically tractable, closed-form models is desirable for several reasons. In communication applications, these properties are essential for deriving capacity, mutual information, and optimal detection rules. For medical

This work was funded in part by the German Federal Ministry of Research, Technology and Space (BMFTR) through Project Internet of Bio-Nano-Things (IoBNT), in part by the German Research Foundation (Deutsche Forschungsgemeinschaft, DFG) under GRK 2950 – ProjectID 509922606 and under grant number SCHA 2350/2-1, and in part by the European Union’s Horizon Europe – HORIZON-EIC-2024-PATHFINDEROPEN-01 under grant agreement Project N. 101185661.

applications like early cancer localization, model inversion for source inference requires well-posed, analytical models to ensure solvability. Lastly, simulating large VNs demands tractable models for computational efficiency and interpretability.

Previously, several works addressed channel modeling for MC in VNs. In [6], an analytical model for advective-diffusive molecule transport in VNs under time-varying flow was derived and subsequently extended in [7], [8] through channel capacity analysis and additional transport phenomena. While the model captures relevant environmental effects, it is analytically unwieldy due to the involvement of infinite-dimensional matrices, inversions, and convolutions. Moreover, the analysis in [6]–[8] is limited to tree-like VNs, neglecting multi-path dynamics from signal splitting and recombination at bifurcations and junctions. In [2], a one-dimensional (1-D) VN model is employed for early cancer detection in the CVS. While the study considers multi-path dynamics, it relies on the assumption of a quasi-steady-state concentration inside the VN and is not suitable for time-varying molecule releases. In [9], a graph-based model is proposed for predicting the propagation of degrading microbubbles in a closed-loop VN. While analytically simple, the model remains largely unvalidated, limiting its predictive utility. In [5], we introduced a 1-D model for advective-diffusive molecule transport in VNs, validated through COMSOL Multiphysics® simulations and experiments. However, the model involves convolutions that lack closed-form solutions and require numerical evaluation. As the number of convolutions grows linearly with both the number of paths and the number of vessels per path, analyzing large-scale VNs, as commonly found in the CVS, is computationally demanding and yields limited analytical insight.

In summary, existing VN channel models tend to trade off analytical tractability, physical accuracy, and scalability, without achieving all three. In this paper, we propose a novel closed-form channel model for advective-diffusive MC in VNs that overcomes these limitations by offering a physically grounded, analytically tractable framework suitable for large-scale VN analysis. The *MIGHT* model extends the well-known observation that first passage times (FPTs) in advective-diffusive channels follow the inverse Gaussian (IG) distribution [10] from individual vessels to entire VNs. Ultimately, the received signal can be expressed by a finite sum of weighted IGs, parameterized by the physical properties of the VN. The main contributions of this work can be summarized as follows:

- 1) We derive a novel, closed-form, and analytically tractable model for advective-diffusive hemodynamic molecule transport in VNs, based on mixtures of IGs. The model is validated by comparison with the results from the model in [5] and finite-element simulations in COMSOL.
- 2) For the first time in MC, we analyze the molecule transport in large-scale VNs containing more than 40

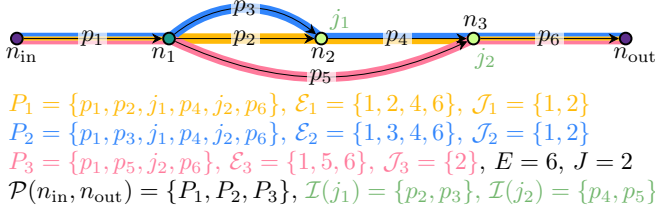


Fig. 1: **Network topology notation.** Exemplary VN with associated notation for the topology.

distinct transport paths, highlighting the model's ability to handle VNs of arbitrary size and complexity.

- 3) Based on the proposed model, we derive a method for the reduction of large VNs to simplified representations that preserve the main transport dynamics.
- 4) We propose a method for the estimation of representative VNs based on the received signal of an unknown VN.

The remainder of this paper is structured as follows: Section II introduces the system model, forming the basis for the derivation and validation of the proposed model in Section III. Section IV provides the analysis of several VNs and presents methods for the structural reduction of VNs and estimation of VN from observed molecular signals. Finally, Section V summarizes the findings and concludes the paper.

II. SYSTEM MODEL

A. Vessel Network Definition

In this work, we adopt a compact version of the VN definition in [5], summarized below. To model molecular transport in VNs, such as the CVS, the network topology is commonly approximated using three segment types (see Fig. 2a)):

- 1) *Pipe*: A pipe p_i is a cylindrical vessel transporting fluid from its inlet to its outlet, defined by its length l_i and radius r_i . Pipes may connect to other pipes, bifurcations, or junctions at both ends.
- 2) *Bifurcation*: A bifurcation is a zero-dimensional connection, where one inflow pipe splits into multiple outflow pipes. It must be connected to pipes on both sides.
- 3) *Junction*: A junction j_m is a zero-dimensional connection, where multiple inflow pipes merge into one outflow pipe. We denote the set of its inflow pipes by $I(j_m)$. As bifurcations, it must be connected to pipes on both sides.

In this paper, we restrict our analysis to networks with a single inlet and a single outlet, denoted by nodes n_{in} and n_{out} , respectively. The extension to networks comprising multiple inlets and outlets is left for future work. All connection points are treated as nodes, and pipes are modeled as directed edges between them, following the flow direction. This representation allows any VN to be described as a directed graph with E pipes and J junctions, see Fig. 2a). We denote the pipe connected to the network outlet n_{out} as p_E . Let $\mathcal{P}(n_{in}, n_{out})$ be the set of all distinct paths from inlet to outlet. Each path P_k comprises a subset of pipes and junctions given by

$$P_k = \{p_i \mid i \in \mathcal{E}_k\} \cup \{j_m \mid m \in \mathcal{J}_k\}, \quad (1)$$

where $\mathcal{E}_k \subseteq \{1, \dots, E\}$ and $\mathcal{J}_k \subseteq \{1, \dots, J\}$ are the index sets of the pipes and junctions included in P_k . The topology-related notation is illustrated for an exemplary VN in Fig. 1.

B. Advective-Diffusive Molecule Transport

A time-invariant flow rate¹ Q at n_{in} establishes a pressure gradient between n_{in} and n_{out} , inducing laminar flow throughout each pipe p_i in the VN, characterized by a flow rate Q_i and a cross-sectional average flow velocity

$$\bar{u}_i = \frac{Q_i}{\pi r_i^2}. \quad (2)$$

The velocities and flow rates in (2) are obtained from an equivalent circuit model, as described in [5]. In addition to advective transport, molecules propagate through the VN via diffusion. Under the assumption of the Aris–Taylor regime, the effective diffusion coefficient in p_i is given by [12, Eq. (26)]

$$\bar{D}_i = \frac{r_i^2 \bar{u}_i^2}{48D} + D \quad (3)$$

and captures the combined effects of molecular diffusion, characterized by the molecular diffusion coefficient D , and shear-induced dispersion resulting from the non-uniform velocity profile across the pipe cross-section. The validity of the Aris–Taylor regime assumption in (2) and (3), and the resulting 1-D modeling, was confirmed in [5] and is further supported by the numerical results in Section III-D.

III. INVERSE GAUSSIAN MIXTURE CHANNEL MODEL

In the following, based on the concept of the FPT, we derive expressions for the molecule flux in both single pipes and paths comprising multiple pipes. An exact solution is obtained for a special case, while for general paths, we find an approximation whose error scales inversely with the Péclet number and which is therefore negligible in the considered regime. Lastly, we generalize the model to entire VNs.

A. Single Pipe Model

When modeling molecular transport by diffusion and flow through a pipe p_i , most works in MC assume molecules are already present at $t = 0$, reflected by the initial condition $c(x, t = 0) = N\delta(x)$ [4], [5], where $c(x, t)$, N , and $\delta(\cdot)$ denotes the molecule concentration at time t and longitudinal position x in p_i , the number of injected molecules, and the Dirac delta function, respectively. In practice, however, molecules typically enter p_i at $t = 0$, either from the preceding pipe, by syringe injection, or by release from nanodevices. Accordingly, in this work, we adopt the more realistic assumption of molecule injection at the pipe inlet $x = 0$ at $t = 0$. We define the FPT as a random variable (RV) describing the time at which a molecule, entering p_i at $x = 0$ and $t = 0$, first reaches position $x = z$, i.e.,

$$T_i(z) = \inf\{t > 0 : x_{T_i} = z \mid x_0 = 0\}, \quad (4)$$

where x_0 and x_{T_i} denote the molecule's positions at $t = 0$ and $t = T_i$, respectively.

Theorem 1. *The FPT $T_i(z)$ at $x = z$ of a single molecule entering pipe p_i at $t = 0$ is IG-distributed, i.e.,*

$$T_i(z) \sim \text{IG}(\mu_i(z), \theta_i(z)), \quad (5)$$

¹Time-invariant blood flow is an accurate approximation in medium-sized and small vessels of the CVS, where pulsatility is damped by the Windkessel effect of the preceding large arteries [11].

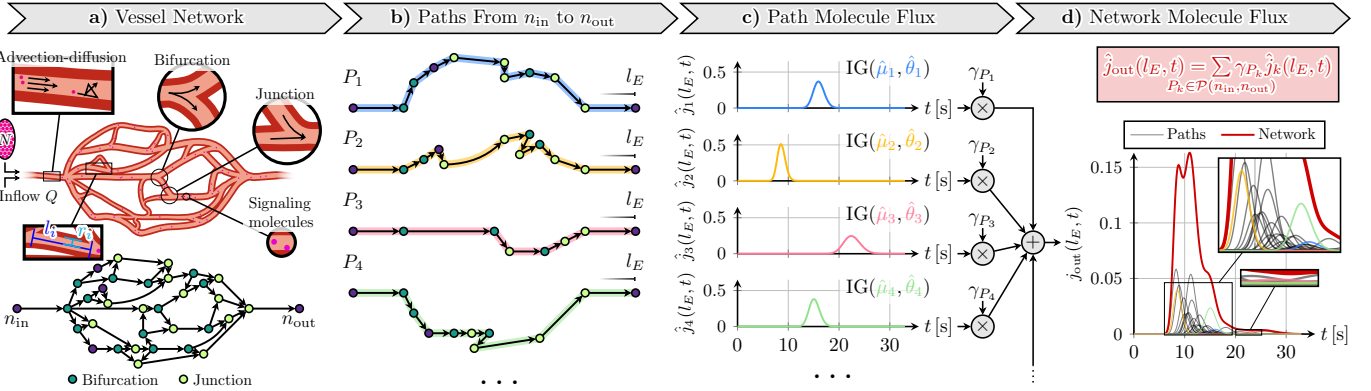


Fig. 2: **System and channel model.** **a)** Molecules released at the inlet n_{in} propagate via advection and diffusion through a VN comprising vessels, bifurcations, and junctions, reaching the outlet n_{out} . The VN is represented as a directed graph. **b)** The VN is decomposed into paths P_k from n_{in} to n_{out} . **c)** The molecule flux at each path outlet follows an IG, parameterized by lengths l_i , radii r_i , and flow velocities \bar{u}_i of the vessels in P_k . **d)** The network flux at the outlet is the sum of path fluxes, weighted by path fractions γ_{P_k} , derived from the flow rates Q_i .

with mean, variance, and scale parameter given by

$$\mu_i(z) = \frac{z}{\bar{u}_i}, \quad \sigma_i^2(z) = \frac{2\bar{D}_i z}{\bar{u}_i^3}, \quad \theta_i(z) = \frac{\sigma_i^2(z)}{\mu_i(z)}. \quad (6)$$

The molecule flux $j_i(z, t)$ in s^{-1} at $x = z$ in p_i is the probability density function (PDF) $f_{IG}(t, z; \mu, \theta)$ of $T_i(z)$ in (5), i.e.,

$$j_i(z, t) = f_{IG}(t, z; \mu_i, \theta_i) = \frac{\mu_i(z)}{\sqrt{2\pi\theta_i(z)t^3}} e^{-\left(\frac{(t-\mu_i(z))^2}{2\theta_i(z)t}\right)}. \quad (7)$$

Proof: The proof is provided in Appendix A.

B. Multiple Pipe Path Model

Building on the model for the flux in a single pipe in Theorem 1, we derive the molecule flux for a path P_k consisting of multiple pipes, see Fig. 2b). Since the propagation in each pipe is modeled as an independent advection–diffusion process, the pipe FPTs $T_i(z)$ in path P_k are mutually independent, i.e., T_i is unaffected by $T_{i'}$, with $i, i' \in \mathcal{E}_k, i \neq i'$. Hence, the path FPT $\bar{T}_k(z)$ of a molecule injected into inlet pipe p_1 at $x = 0$ and $t = 0$, propagating through P_k and reaching $x = z$ in outlet pipe p_E , is the sum of the individual pipe FPTs

$$\bar{T}_k(z) = \sum_{i \in \mathcal{E}_k \setminus \{E\}} T_i(l_i) + T_E(z). \quad (8)$$

Therefore, the path flux $\bar{j}_k(z, t)$ at $x = z$ in outlet pipe p_E can be obtained by convolving the pipe PDFs in (7)

$$\bar{j}_k(z, t) = (*_{i \in \mathcal{E}_k \setminus \{E\}} j_i(l_i, t)) * j_E(z, t), \quad (9)$$

where $*_{i \in \mathcal{E}_k \setminus \{E\}}$ denotes the temporal convolution of all pipe fluxes j_i at their outlets l_i in path P_k , except outlet pipe p_E , and $*$ denotes a single convolution with respect to (w.r.t.) time. Below, we derive two closed-form expressions for (9).

Theorem 2. For the special case of homogeneous parameters in pipes $p_i \in P_k$, i.e., $\bar{u}_i = \bar{u}$ and $\bar{D}_i = \bar{D}$, the path FPT $\bar{T}_k(z)$ of a molecule injected at $x = 0$, $t = 0$ and reaching $x = z$ in outlet pipe p_E is again IG-distributed

$$\bar{T}_k(z) = \tilde{T}_k(z) \sim IG(\tilde{\mu}_k(z), \tilde{\theta}_k(z)), \quad (10)$$

with path mean, variance, and scale parameter given by

$$\tilde{\mu}_k(z) = \frac{\bar{l}_k(z)}{\bar{u}}, \quad \tilde{\sigma}_k^2(z) = \frac{2\bar{D}\bar{l}_k(z)}{\bar{u}^3}, \quad \tilde{\theta}_k(z) = \frac{\tilde{\sigma}_k^2(z)}{\tilde{\mu}_k(z)}, \quad (11)$$

where $\bar{l}_k(z)$ is the path length, defined by the pipe lengths l_i of the pipes $p_i \in P_k$ and position z in outlet pipe p_E , i.e., $\bar{l}_k(z) = \sum_{i \in \mathcal{E}_k \setminus \{E\}} l_i + z$. The PDF of $\tilde{T}_k(z)$ is given as $\hat{j}_k(z, t) = f_{IG}(t, z; \tilde{\mu}_k, \tilde{\theta}_k)$, see (7).

Proof: The proof is provided in Appendix B.

For the general case of heterogeneous pipe parameters, where l_i, r_i, \bar{u}_i , and \bar{D}_i vary across the pipes $p_i \in P_k$, the path FPT $\bar{T}_k(z)$ in outlet pipe p_E is not exactly IG-distributed. However, by applying the method of moment matching, $\bar{T}_k(z)$ can be approximated by an IG-distributed RV $\hat{T}_k(z)$

$$\bar{T}_k(z) \approx \hat{T}_k(z) \sim IG(\hat{\mu}_k(z), \hat{\theta}_k(z)), \quad (12)$$

whose mean $\hat{\mu}_k(z)$ and variance $\hat{\sigma}_k^2(z)$ exactly matches those of the true path FPT $\bar{T}_k(z)$. Since all pipe FPTs in (8) are independent RVs, the mean $\bar{\mu}_k(z)$ and variance $\bar{\sigma}_k^2(z)$ of the true path FPT $\bar{T}_k(z)$ are obtained by summing the means and variances of the individual pipe FPTs, which are matched to the moments of $\hat{T}_k(z)$ as follows

$$\begin{aligned} \hat{\mu}_k(z) &= \bar{\mu}_k(z) = \mu_E(z) + \sum_{i \in \mathcal{E}_k \setminus \{E\}} \mu_i(l_i), \\ \hat{\sigma}_k^2(z) &= \bar{\sigma}_k^2(z) = \sigma_E^2(z) + \sum_{i \in \mathcal{E}_k \setminus \{E\}} \sigma_i^2(l_i), \end{aligned} \quad (13)$$

with $\hat{\theta}_k(z) = \hat{\sigma}_k^2(z)/\hat{\mu}_k(z)$. Consequently, for heterogeneous path parameters, the path flux $\bar{j}_k(z, t)$ can be represented by $\hat{j}_k(z, t)$, obtained from the PDF in (7) with the matched moments in (13), i.e., $\bar{j}_k(z, t) \approx \hat{j}_k(z, t) = f_{IG}(t, z; \hat{\mu}_k, \hat{\theta}_k)$.

Theorem 3. The approximation in (12) is exact w.r.t. the first two moments and asymptotically exact w.r.t. the third moment for large Péclet numbers. In particular, the error $\Delta\xi = \bar{\xi}_k - \hat{\xi}_k$ in the skewness $\bar{\xi}_k$ of \bar{T}_k and $\hat{\xi}_k$ of \hat{T}_k scales as

$$\Delta\xi \propto \frac{1}{\sqrt{Pe_k}}, \quad (14)$$

where Pe_k is the path Péclet number, i.e., $Pe_k = 2\bar{\mu}_k/\bar{\theta}_k$.

Proof: The proof is provided in Appendix C.

The validity of the approximation $\bar{j}_k(z, t) \approx \hat{j}_k(z, t)$ is confirmed by comparison to the convolution in (9), the model in [5], and finite-element simulations in COMSOL in Subsection III-D. We note that moderately large Pe_k (e.g., $1 \ll Pe_k \ll 10^4$) are required for the Aris-Taylor regime to

hold, in which case the molecule flux usually exhibits no skewness in t and $\Delta\xi$ becomes negligibly small.

C. Vessel Network Model

Considering a general VN consisting of multiple paths $P_k \in \mathcal{P}(n_{\text{in}}, n_{\text{out}})$ with heterogeneous pipe parameters, the molecule flux j_{out} at position z in VN outlet pipe p_E in s^{-1} is the weighted sum of the path fluxes (see Figs. 2c) and 2d), i.e.,

$$j_{\text{out}}(z, t) = \sum_{P_k \in \mathcal{P}(n_{\text{in}}, n_{\text{out}})} \gamma_{P_k} \bar{j}_k(z, t), \quad (15)$$

where [2, Eq. (22)]

$$\gamma_{P_k} = \prod_{\substack{p_i, j_m \in P_k \\ p_i \in \mathcal{I}(j_m)}} \frac{Q_i}{\sum_{p_v \in \mathcal{I}(j_m)} Q_v}, \quad 0 \leq \gamma_{P_k} \leq 1, \quad (16)$$

denotes the fraction of molecules propagating through path P_k , dictated by the fractions of flow rates at each junction $j_m \in P_k$. Unlike the model in [5, Eq. (8)], (15) contains no convolutions. It provides a tractable and insightful closed-form expression for the molecule flux in VNs, in which the contributions of different paths can be easily identified. By dividing (15) by the flow velocity \bar{u}_E in VN outlet pipe p_E , and multiplying with N , the molecule concentration in m^{-1} is obtained as

$$c_{\text{out}}(z, t) \approx \frac{N}{\bar{u}_E} j_{\text{out}}(z, t). \quad (17)$$

This assumes negligible diffusive flux at n_{out} compared to advective flux, which holds for $\text{Pe}_k \gg 1$, i.e., in the Aris-Taylor regime. This assumption is validated in Subsection III-D.

To focus on the channel characteristics, we assume a perfect counting receiver (RX) of length l_{RX} , centered at z_{RX} in the outlet pipe p_E , which yields the number of molecules observed in the RX domain as received signal

$$N_{\text{obs}}(t) = \int_{z_{\text{RX}} - l_{\text{RX}}/2}^{z_{\text{RX}} + l_{\text{RX}}/2} c_{\text{out}}(z, t) dz \approx l_{\text{RX}} c_{\text{out}}(z_{\text{RX}}, t). \quad (18)$$

The latter approximation is valid under the uniform concentration assumption (UCA) [4].

D. Model Validation

To validate the proposed MIGHT model, in Fig. 3, we compare the predicted $N_{\text{obs}}(t)$ in (18) for various VN topologies to three benchmarks: The convolution-based model from [5], the exact numerical convolution of pipe fluxes in (9), and finite-element simulations performed in COMSOL. COMSOL simulations were carried out in 3-D space, using the laminar flow and particle tracing modules with Brownian motion.

Fig. 3 shows the comparison for three VNs of increasing complexity. In all cases, $D = 1.461 \times 10^{-7} \text{ m}^2 \text{ s}^{-1}$ was used, motivated by experimental observations in [13]. All other VN parameters are provided in Fig. 3. In Figs. 3a) and 3b), $N_{\text{obs}}(t)$ exhibits two and three distinct peaks, respectively, corresponding to the number of available paths between n_{in} and n_{out} . These distinct peaks are only visible if the delays induced by the paths are sufficiently different and each path carries a significant fraction of the total number of molecules. Fig. 3c) features a larger VN with seven paths between n_{in} and n_{out} and curved vessels. In this example, most path contributions overlap and only one distinct peak is visible. For all considered VNs, we can observe that the closed-form model based on the mixture of IG distributions, proposed in Section III-C,

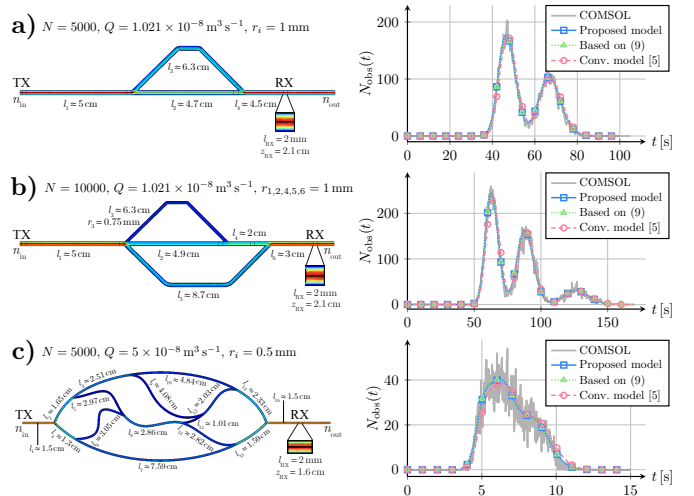


Fig. 3: **Model validation.** $N_{\text{obs}}(t)$ simulated in COMSOL, predicted by (18), the convolution in (9), and the convolution-based model from [5] for different VNs. COMSOL velocity magnitudes are color-coded on the left to indicate flow patterns qualitatively.

is in excellent agreement with the numerical convolution of path fluxes in (9) and the results obtained from COMSOL simulations. Furthermore, the proposed model is in excellent agreement with the convolution-based model from [5] for the VNs in Figs. 3a) and 3b). For the more complex VN in Fig. 3c), it can be observed that the proposed model is more accurate than the model from [5], which is not able to accurately reproduce the decay of the signal. Overall, our analysis confirms the validity of the MIGHT model for describing hemodynamic molecule transport in complex VNs. Across all validation scenarios, for all paths P_k , Pe_k is moderately large and ranges from 74.4 to 211.6, making the skewness error $\Delta\xi$ in (14) negligible and further confirming the validity of Theorem 3.

IV. APPLICATIONS OF PROPOSED MODEL

We demonstrate the MIGHT model's utility for two application scenarios: The structural reduction of VNs and the estimation of representative networks from observed signals. This is illustrated for three additional VNs of varying complexity (see Fig. 4), chosen as physiologically plausible but anatomically abstract test cases. Future work will address anatomically accurate VNs derived from imaging data.

A. Vessel Network Reduction

In most VNs, only certain parts of the topology contribute significantly to the received signal, while others have negligible influence. Thus, we propose an approach for the systematic reduction of VNs to simplified representations that preserve the essential signal properties. This reduction can facilitate the interpretation of transport dynamics, lower computational cost in large-scale simulations, may lead to surrogate models that capture the behavior of entire organs or tissues without requiring vessel-level detail, and enable efficient parameter estimation or the design of microfluidic testbeds that reproduce dominant transport characteristics of complex VNs.

To derive a reduced VN, we first compute the fraction of molecules propagating through each pipe p_i

$$\gamma_{p_i} = \sum_{\{P_k | p_i \in P_k\}} \gamma_{P_k}, \quad 0 \leq \gamma_{p_i} \leq 1. \quad (19)$$

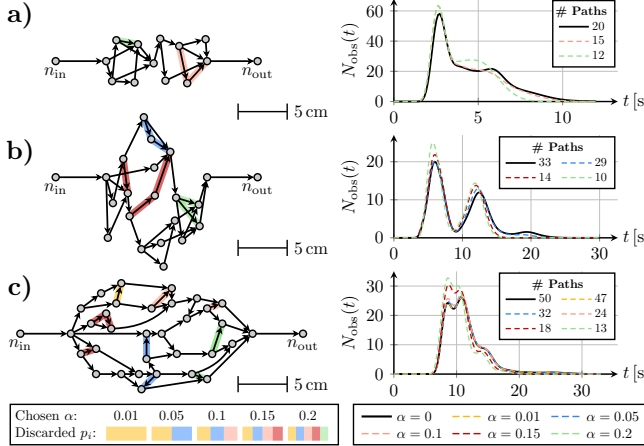


Fig. 4: **Structural reduction of VNs.** For each VN, the original topology and the discarded pipes, as well as the resulting $N_{\text{obs}}(t)$ are shown for various α . Pipe lengths are depicted to scale. In a) and b), radii were drawn from a normal distribution with mean 0.5 mm and standard deviation 0.1 mm. In c), $r_i = 0.5$ mm.

All γ_{p_i} and associated pipes are then sorted in descending order, and pipes in the lower α -quantile are discarded, retaining only the most significant parts of the network. The parameter $\alpha \in [0, 1]$ controls the degree of reduction.

The VN reduction is illustrated in Fig. 4 for various VNs and α -values, with $N = 10000$, $Q = 1 \times 10^{-7} \text{ m}^3 \text{ s}^{-1}$, $D = 1.461 \times 10^{-7} \text{ m}^2 \text{ s}^{-1}$, $z_{\text{RX}} = 2.1 cm, and $l_{\text{RX}} = 2$ mm. We observe that larger α result in more aggressive pruning. For all VNs, appropriate α substantially reduce VN complexity while preserving the overall transport dynamics. The number of paths between n_{in} and n_{out} can often be halved without markedly affecting molecular transport. Since the removal of a single pipe potentially eliminates multiple paths, a far stronger reduction in the number of paths than in the number of vessels is generally possible.$

B. Estimating Vessel Networks from Signals

Estimating a representative VN from an observed molecular signal is crucial for many envisioned MC applications, especially since patient-specific vascular topologies are generally unknown. Such estimates could enable precision medicine, e.g., by tumor localization from biomarker signals or yield simplified VNs with comparable transport dynamics, useful for designing microfluidic chips that mimic organ dynamics. In the following, leveraging the analytical tractability of the MIGHT model, derived in Section III, we propose a method for estimating a simplified VN that reproduces the behavior of an unknown complex VN underlying an observed signal $r(t)$.

Let $r(t)$ denote a molecular signal (e.g., $N_{\text{obs}}(t)$, flux, or concentration) observed at n_{out} of an unknown VN. To estimate a representative VN that reproduces $r(t)$, we proceed in two steps. First, we fit the IG mixture in (15) with M components to $r(t)$. Second, we synthesize a *prototype VN* capable of producing the mixture that has been estimated in the first step.

In the **fitting step**, we fit an IG flux mixture with M components, whose mean, scale, and weight parameters are collected in vectors $\bar{\mu} = [\bar{\mu}_1, \dots, \bar{\mu}_M]^T$, $\bar{\theta} = [\bar{\theta}_1, \dots, \bar{\theta}_M]^T$,

and $\gamma = [\gamma_{P_1}, \dots, \gamma_{P_M}]^T$, respectively, to $r(t)$ according to

$$\begin{aligned} \{\bar{\mu}^*, \bar{\theta}^*, \gamma^*\} &= \arg \min_{\bar{\mu}, \bar{\theta}, \gamma} \int_0^\infty \left(r(t) - a \sum_{k=1}^M \gamma_{P_k} \bar{j}_k(l_E, t) \Big|_{\bar{\mu}_k, \bar{\theta}_k} \right)^2 dt \\ \text{s.t. } \forall k : \gamma_{P_k} &\geq 0, \quad \sum_{k=1}^M \gamma_{P_k} = 1. \end{aligned} \quad (20)$$

Here, $|$ denotes the *evaluated at* operator and a is a scaling factor that may be needed to translate the fitted flux signal to a concentration or $N_{\text{obs}}(t)$, see (17) and (18). The optimal parameters of the mixture are collected in $\bar{\mu}^*$, $\bar{\theta}^*$, and γ^* .

In the second step, a prototype VN is **synthesized** that can produce the optimal parameters found in the fitting step. In this work, we assume the prototype VN topology in Fig. 5a), with M parallel paths between n_{in} and n_{out} . Subsequently, we find the l_i and r_i for all p_i in the VN such that $\bar{\mu}^*$, $\bar{\theta}^*$, γ^* found in (20) are closely reproduced, i.e., we solve

$$\begin{aligned} \{l_1^*, \dots, l_E^*, r_1^*, \dots, r_E^*\} &= \arg \min_{\{l_1, \dots, l_E, r_1, \dots, r_E\}} \\ &\sum_{k=1}^M (\bar{\mu}_k - \bar{\mu}_k^*)^2 + w_\theta (\bar{\theta}_k - \bar{\theta}_k^*)^2 + w_\gamma (\gamma_{P_k} - \gamma_{P_k}^*)^2 \\ \text{s.t. } \forall k : \bar{u}_1 &= \frac{Q}{\pi r_1^2}, \quad \bar{u}_E = \frac{Q}{\pi r_E^2}, \quad \bar{u}_{k+1} = \frac{Q}{\pi r_{k+1}^2} \frac{r_{k+1}^4 / l_{k+1}}{\sum_{\kappa=1}^M r_\kappa^4 / l_\kappa}, \\ \bar{\mu}_k &= \mu_1 + \mu_{k+1} + \mu_E, \quad \bar{\sigma}_k^2 = \sigma_1^2 + \sigma_{k+1}^2 + \sigma_E^2, \quad \bar{\theta}_k = \frac{\sigma_k^2}{\bar{\mu}_k}, \end{aligned} \quad (21)$$

where the weights $w_\theta \geq 0$ and $w_\gamma \geq 0$ are chosen such that $\bar{\mu}_k$, $\bar{\theta}_k$, and γ_{P_k} contribute on comparable scales to the objective function. For simplicity, we drop the argument $z = l_E$ in (21). We solve (21) using SciPy's Trust Region Reflective algorithm.

Since (21) is a non-linear problem, suitable l_i^* and r_i^* yielding $\bar{\mu}^*$, $\bar{\theta}^*$, γ^* may not always be found directly. In such cases, a **correction step** adds degrees of freedom by splitting the path P_k with the highest γ_{P_k} into L_k sub-components of equal $\bar{\mu}_k$ and $\bar{\theta}_k$ but reduced weights $\gamma'_{P_k} \leftarrow \gamma_{P_k} / L_k$. This step can be repeated until a suitable prototype VN is identified.

Fig. 5 shows the $N_{\text{obs}}(t)$ signals of four previously introduced VNs, the signals resulting from the IG fitting step, the parameters of the estimated VNs, and their respective $N_{\text{obs}}(t)$ signals. We observe that the estimated VNs closely reproduce the original signals in all cases, with lengths and radii in the same order of magnitude as in the VNs underlying the observed signals. In Fig. 5b), fitted and estimated signals coincide and the underlying VN shares the same topology as the prototype (see Figs. 3a) and 5a)). In Figs. 5c)–e), the estimated VNs contain far fewer paths than the originals, demonstrating that a few dominant paths suffice to capture complex VN behavior. In Figs. 5d) and 5e), p_5 and p_6 take on identical values, as their mean and scale parameters coincide due to the correction step enforcing smaller weights. Overall, these results confirm the feasibility of VN estimation using the proposed approach.

V. CONCLUSION

In this paper, we proposed a novel model for advective-diffusive MC in complex VNs, derived from first principles and based on the concept of the FPT. The MIGHT model expresses network-wide transport dynamics as a weighted sum

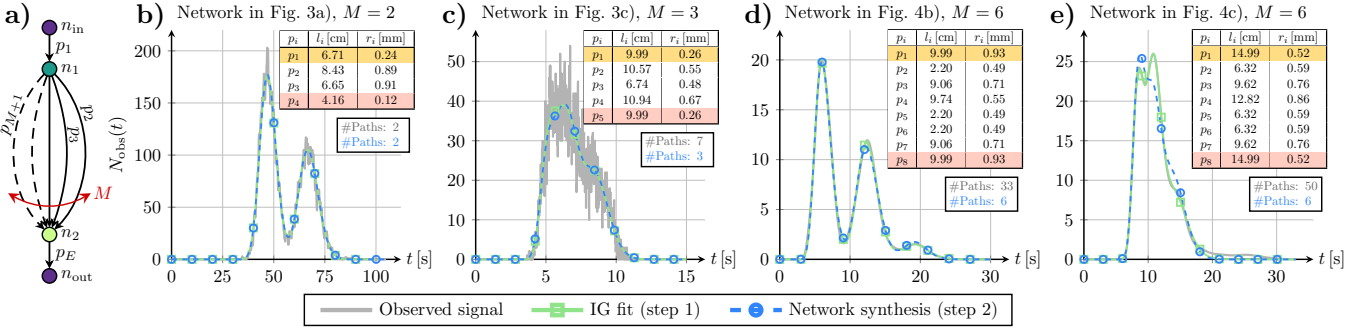


Fig. 5: VN estimation. a) Prototype VN. b)–e) Estimated VNs from COMSOL data (b, c)) and synthetic signals (d, e)) reproduce the observed signals across different VN sizes. Fitted IG signals and estimated outputs are shown in green and blue, respectively. The numbers of paths in the original and estimated VNs are shown in gray and blue in the subplots. Inlet and outlet pipes are highlighted in yellow and rose.

of IG distributions. Its accuracy was validated against finite-element simulations in COMSOL and the convolution-based model in [5], for VNs of varying complexity. Leveraging the model’s analytical tractability, we further proposed methods for the structural reduction of VNs and the estimation of simplified VNs that replicate molecular signals from unknown topologies. In summary, the MIGHT model combines physical accuracy with analytical tractability and constitutes a practical tool for analyzing, simplifying, and inferring VNs in MC.

Future work may extend the model to include sorption at vessel walls and closed-loop VNs, enabling the study of intersymbol interference and MC in patient-derived VNs.

APPENDIX

A. Proof of Theorem 1

Proof. The 1-D advection-diffusion equation for a pipe p_i where a single molecule enters at $x = 0$ at time $t = 0$ is given by

$$\partial_t c_i(x, t) = \bar{D}_i \partial_{xx} c_i(x, t) - \bar{u}_i \partial_x c_i(x, t), \quad (22)$$

with the initial condition $c_i(x, 0) = 0$ and the influx boundary condition at the pipe inlet

$$-\bar{D}_i \partial_x c_i(0, t) + \bar{u}_i c_i(0, t) = \delta(t), \quad (23)$$

where ∂_t and ∂_x denote the first partial derivative w.r.t. t and x , respectively, and ∂_{xx} denotes the second partial derivative w.r.t. x .

By applying the one-sided Laplace transform w.r.t. t , denoted by $\mathcal{L}\{\cdot\}$, and exploiting the initial condition $c_i(x, 0) = 0$, (22) can be transformed into the frequency domain as follows

$$\bar{D}_i \partial_{xx} C_i(x, s) - \bar{u}_i \partial_x C(x, s) - s C_i(x, s) = 0, \quad (24)$$

where s denotes the complex frequency variable of the Laplace transform and $C_i(x, s) = \mathcal{L}\{c_i(x, t)\}$ denotes the Laplace-transformed concentration.

Next, we assume a standard solution for the concentration $C_i(x, s)$ in the Laplace domain of the form

$$C_i(x, s) = A_i(s) e^{\lambda_i(s, \bar{u}_i, \bar{D}_i)x}. \quad (25)$$

Inserting (25) into (24) and solving for the λ_i -values leads to

$$\lambda_i(s, \bar{u}_i, \bar{D}_i) = \frac{\bar{u}_i \pm \sqrt{\bar{u}_i^2 + 4\bar{D}_i s}}{2\bar{D}_i}. \quad (26)$$

Since $c_i(x, t) \rightarrow 0$ for $t \rightarrow \infty$, we only consider the λ_i -values in (26) with a minus sign in the \pm -operator.

To obtain $A_i(s)$, we insert (25) into the Laplace transform of boundary condition (23), leading to

$$-\bar{D}_i \lambda_i A_i(s) + \bar{u}_i A_i(s) = 1 \Leftrightarrow A_i(s) = \frac{1}{\bar{u}_i - \bar{D}_i \lambda_i}, \quad (27)$$

where we dropped the arguments of λ_i for better readability. Inserting (26) and (27) into (25) yields a solution for $C_i(x, s)$.

Subsequently, we derive a solution for the advective-diffusive flux $j_i(x, t)$ in pipe p_i , defined as

$$j_i(x, t) = \bar{u}_i c_i(x, t) - \bar{D}_i \partial_x c_i(x, t). \quad (28)$$

An expression for $J_i(x, s) = \mathcal{L}\{j_i(x, t)\}$ in the Laplace domain can be obtained by transforming (28) into the Laplace domain, inserting $C_i(x, s)$ from (25), and solving for the flux $J_i(x, s)$ as follows

$$\begin{aligned} J_i(x, s) &= \bar{u}_i C_i(x, s) - \bar{D}_i \partial_x C_i(x, s) \\ &= \underbrace{(\bar{u}_i - \lambda_i \bar{D}_i)}_{A_i^{-1}(s)} A_i(s) e^{\lambda_i x} = e^{\lambda_i x}. \end{aligned} \quad (29)$$

Next, we obtain the time-domain flux $j_i(x, t)$ by applying the inverse one-sided Laplace transform $\mathcal{L}^{-1}\{\cdot\}$ to (29):

$$j_i(x, t) = \mathcal{L}^{-1}\{J_i(x, s)\} = \frac{x}{\sqrt{4\pi \bar{D}_i t^3}} e^{\left(-\frac{(x-\bar{u}_i t)^2}{4\bar{D}_i t}\right)}. \quad (30)$$

Exploiting the definitions for the mean, variance, and scale parameter from (6), (30) evaluated at $x = z$ follows as

$$\begin{aligned} j_i(z, t) &= \frac{z}{\sqrt{4\pi \bar{D}_i t^3}} e^{\left(-\frac{(z-\bar{u}_i t)^2}{4\bar{D}_i t}\right)} = \frac{\frac{z}{\bar{u}_i}}{\sqrt{2\pi \frac{2\bar{D}_i}{\bar{u}_i^2} t^3}} e^{\left(-\frac{(t-\frac{z}{\bar{u}_i})^2}{2\bar{D}_i t}\right)} \\ &= \frac{\mu_i(z)}{\sqrt{2\pi \theta_i(z) t^3}} e^{\left(-\frac{(t-\mu_i(z))^2}{2\theta_i(z) t}\right)} = f_{\text{IG}}(t, z; \mu_i, \theta_i), \end{aligned} \quad (31)$$

which exactly matches the PDF of the IG distribution in (7). This concludes the the proof. \square

B. Proof of Theorem 2

Proof. Applying the one-sided Laplace transform w.r.t. x to the path flux $\bar{j}_k(x = z, t)$ in (9) converts the convolutions in the time domain into multiplications in the frequency domain

$$\mathcal{L}\{\bar{j}_k(z, t)\} = \bar{J}_k(z, s) = J_E(z, s) \cdot \prod_{i \in \mathcal{E}_k \setminus \{E\}} J_i(l_i, s). \quad (32)$$

Inserting (29) into (32) yields

$$\bar{J}_k(z, s) = e^{\left(\sum_{i \in \mathcal{E}_k \setminus \{E\}} \lambda_i(s, \bar{u}_i, \bar{D}_i) l_i + \lambda_E(s, \bar{u}_E, \bar{D}_E) z\right)}. \quad (33)$$

For homogeneous parameters in pipes $p_i \in P_k$, i.e., $\bar{u}_i = \bar{u}$ and $\bar{D}_i = \bar{D}$, all λ -values in (33) are equal, i.e.,

$$\begin{aligned} \lambda_i(s, \bar{u}_i, \bar{D}_i) &= \lambda_E(s, \bar{u}_E, \bar{D}_E) \\ &= \frac{\bar{u} - \sqrt{\bar{u}^2 + 4\bar{D}s}}{2\bar{D}} = \lambda(s, \bar{u}, \bar{D}), \end{aligned} \quad (34)$$

and the path flux in the Laplace domain follows as

$$\bar{J}_k(z, s) = e^{\left(\lambda(s, \bar{u}, \bar{D})\left(\sum_{i \in \mathcal{E}_k \setminus \{E\}} l_i + z\right)\right)} = e^{\left(\lambda(s, \bar{u}, \bar{D})\bar{l}_k(z)\right)}, \quad (35)$$

where $\bar{l}_k(z)$ is the effective path length given below (11). Taking the inverse Laplace transform of (35), and applying the modifications already used in (31) exactly yields the PDF of an IG distribution with mean, variance, and scale parameter according to (11). This concludes the proof. \square

C. Proof of Theorem 3

For a more compact mathematical description, and without loss of generality, below, we evaluate all variables concerning any pipe p_i (including pipe p_E) at the pipes' outlets and drop the explicit positional argument for better readability.

Proof. First, we consider the FPT T_i of a single pipe p_i and derive the the moment generating function (MGF) as

$$\begin{aligned} M_{T_i}(s) &= E[e^{sT_i}] = \int_0^\infty e^{st} f_{IG}(t, x; \mu_i, \theta_i) dt = \\ &= e^{\left(\frac{\mu_i}{\theta_i}(1 - \sqrt{1 - 2\theta_i s})\right)}, \end{aligned} \quad (36)$$

where $E[\cdot]$ denotes the expectation operator. From the MGF, the cumulant generating function (CGF) can be obtained as

$$K_{T_i}(s) = \log M_{T_i}(s) = \frac{\mu_i}{\theta_i}(1 - \sqrt{1 - 2\theta_i s}). \quad (37)$$

From (37), the first three cumulants of T_i follow as

$$\begin{aligned} \kappa_1(T_i) &= K'_{T_i}(0) = \mu_i, & \kappa_2(T_i) &= K''_{T_i}(0) = \mu_i \theta_i \\ \kappa_3(T_i) &= K'''_{T_i}(0) = 3\mu_i \theta_i^2, \end{aligned} \quad (38)$$

where $K'_{T_i}(0)$, $K''_{T_i}(0)$ and $K'''_{T_i}(0)$ denote the first, second, and third derivative of $K_{T_i}(s)$ w.r.t. s , evaluated at $s = 0$. Then, from the first three cumulants in (38), the first three moments of T_i are obtained as

$$E[T_i] = \kappa_1(T_i) = \mu_i, \quad (39)$$

$$\text{Var}[T_i] = \kappa_2(T_i) = \mu_i \theta_i = \sigma_i^2, \quad (40)$$

$$\text{Skew}[T_i] = \xi_i = \frac{\kappa_3(T_i)}{\kappa_2^{3/2}(T_i)} = 3\sqrt{\frac{\theta_i}{\mu_i}}, \quad (41)$$

where $\text{Var}[\cdot]$ and $\text{Skew}[\cdot]$ denote the variance and skewness operator, respectively. (39) and (40) confirm the moments provided in (6) for a single pipe.

Based on the cumulants and moments of a single pipe p_i , below, we first derive the skewness of the true path FPT \bar{T}_k in (8), and subsequently the skewness of the approximated path FPT \hat{T}_k in (12). As all pipe FPTs are mutually independent (see Section III-B), \bar{T}_k is the sum of the individual pipe FPTs T_i (see (8)), and the path PDF is obtained by convolution of the individual pipe PDFs (see (9)). Hence, for the moment

and cumulant generating functions as well as the cumulants, it follows that

$$M_{\bar{T}_k}(s) = \prod_{i \in \mathcal{E}_k} M_{T_i}(s), \quad K_{\bar{T}_k}(s) = \sum_{i \in \mathcal{E}_k} K_{T_i}(s), \quad (42)$$

$$\bar{\kappa}_m(\bar{T}_k) = \sum_{i \in \mathcal{E}_k} \kappa_m(T_i), \quad \forall m \geq 1. \quad (43)$$

Then, the skewness of the true path FPT \bar{T}_k in (8) can be derived from the definition of the skewness in (41) and the path cumulants in (43) as

$$\begin{aligned} \text{Skew}[\bar{T}_k] &= \bar{\xi}_k = \frac{\bar{\kappa}_3(\bar{T}_k)}{\bar{\kappa}_2^{3/2}(\bar{T}_k)} = \frac{\sum_{i \in \mathcal{E}_k} \kappa_3(T_i)}{\left(\sum_{i \in \mathcal{E}_k} \kappa_2(T_i)\right)^{3/2}} \\ &= 3 \frac{\sum_{i \in \mathcal{E}_k} \mu_i \theta_i^2}{\left(\sum_{i \in \mathcal{E}_k} \mu_i \theta_i\right)^{3/2}}. \end{aligned} \quad (44)$$

For the approximated path FPT \hat{T}_k in (12) of path P_k , the skewness $\hat{\xi}_k$ cannot be derived directly from the cumulants, but is implicitly defined by the matched moments in (13) as

$$\text{Skew}[\hat{T}_k] = \hat{\xi}_k = 3\sqrt{\frac{\hat{\theta}_k}{\hat{\mu}_k}} \stackrel{(13)}{=} 3\sqrt{\frac{\sum_{i \in \mathcal{E}_k} \mu_i \theta_i}{\sum_{i \in \mathcal{E}_k} \mu_i}}. \quad (45)$$

In the last part of the proof, we derive an expression for the error $\Delta\xi$ between the skewness of the true (44) and of the approximated (45) path FPT of path P_k , i.e.,

$$\Delta\xi = \bar{\xi}_k - \hat{\xi}_k. \quad (46)$$

To obtain a tractable expression, we define the relative weights

$$w_i := \frac{\mu_i}{\sum_{j \in \mathcal{E}_k} \mu_j} = \frac{\mu_i}{\hat{\mu}_k} \quad \text{with} \quad \sum_{i \in \mathcal{E}_k} w_i = 1, \quad (47)$$

where the denominator is equivalent to the matched path mean in (13). Further, we define the weighted mean of the θ_i -values as

$$m_1 := \sum_{i \in \mathcal{E}_k} w_i \theta_i = \frac{\sum_{i \in \mathcal{E}_k} \mu_i \theta_i}{\hat{\mu}_k} = \hat{\theta}_k, \quad (48)$$

which is equivalent to the matched path scale parameter in (13). Exploiting this, we can define the weighted variance of the θ_i -values as

$$\text{Var}_w(\theta_i) := \sum_{i \in \mathcal{E}_k} w_i (\theta_i - m_1)^2. \quad (49)$$

Using (47)–(49), the expressions for the true (44) and approximated (45) path FPT can be reformulated as

$$\bar{\xi}_k = 3 \frac{\sum_{i \in \mathcal{E}_k} \mu_i \theta_i^2}{\left(\sum_{i \in \mathcal{E}_k} \mu_i \theta_i\right)^{3/2}} = 3 \frac{\bar{\mu}_k \sum_{i \in \mathcal{E}_k} w_i \theta_i^2}{\bar{\mu}_k^{3/2} m_1^{3/2}} = \frac{3}{\sqrt{\bar{\mu}_k}} \frac{\sum_{i \in \mathcal{E}_k} w_i \theta_i^2}{m_1^{3/2}},$$

$$\hat{\xi}_k = 3 \frac{\sqrt{\sum_{i \in \mathcal{E}_k} \mu_i \theta_i}}{\sum_{i \in \mathcal{E}_k} \mu_i} = 3 \frac{\sqrt{\hat{\mu}_k m_1}}{\hat{\mu}_k} = \frac{3}{\sqrt{\hat{\mu}_k}} \sqrt{m_1}. \quad (50)$$

Inserting these expressions into (46), and exploiting (47)–(49), and $\hat{\mu}_k = \bar{\mu}_k$ (see (13)), it follows that

$$\begin{aligned} \Delta\xi &= \bar{\xi}_k - \hat{\xi}_k \stackrel{(47),(48)}{=} \frac{3}{\sqrt{\hat{\mu}_k}} \left[\frac{\sum_{i \in \mathcal{E}_k} w_i \theta_i^2}{m_1^{3/2}} - \sqrt{m_1} \right] \\ &= \frac{3}{\sqrt{\hat{\mu}_k}} \frac{\sum_{i \in \mathcal{E}_k} w_i \theta_i^2 - m_1^2}{m_1^{3/2}} \stackrel{(49)}{=} \frac{3}{\sqrt{\hat{\mu}_k}} \frac{\text{Var}_w(\theta_i)}{m_1^{3/2}} \\ &= 3 \frac{\text{Var}_w(\theta_i)}{m_1^2} \sqrt{\frac{\hat{\theta}_k}{\hat{\mu}_k}}. \end{aligned} \quad (51)$$

Finally, by inserting the definition of the path Péclet number $\text{Pe}_k = 2\hat{\mu}_k/\hat{\theta}_k$ into (51), the error $\Delta\xi$ between the true (44) and approximated skewness (45) follows as

$$\Delta\xi = \bar{\xi}_k - \hat{\xi}_k = 3 \frac{\text{Var}_w(\theta_i)}{m_1^2} \sqrt{\frac{2}{\text{Pe}_k}} \propto \frac{1}{\sqrt{\text{Pe}_k}}, \quad (52)$$

which is inversely proportional to the path Péclet number Pe_k . From this, it is evident that the proposed MIGHT model is physically accurate at large path Péclet numbers, e.g., as assumed in the Aris-Taylor regime. This concludes the proof. \square

REFERENCES

- [1] I. Akyildiz *et al.*, “The Internet of Bio-Nano Things,” *IEEE Commun. Mag.*, vol. 53, pp. 32–40, Mar. 2015.
- [2] R. Mosayebi *et al.*, “Early cancer detection in blood vessels using mobile nanosensors,” *IEEE Trans. Nanobiosci.*, vol. 18, pp. 103–116, Apr. 2019.
- [3] U. A. K. Chude-Okonkwo *et al.*, “Molecular communication and nanonetwork for targeted drug delivery: A survey,” *IEEE Commun. Surv. Tutor.*, vol. 19, no. 4, pp. 3046–3096, 2017.
- [4] V. Jamali, A. Ahmadzadeh, W. Wicke, A. Noel, and R. Schober, “Channel modeling for diffusive molecular communication—A tutorial review,” *Proc. IEEE*, vol. 107, no. 7, pp. 1256–1301, Jul. 2019.
- [5] T. Jakumeit, L. Brand, J. Kirchner, R. Schober, and S. Lotter, “Molecular signal reception in complex vessel networks: The role of the network topology,” in *Proc. IEEE Int. Conf. Commun.*, Jun. 2024.
- [6] Y. Chahibi, M. Pierobon, S. O. Song, and I. F. Akyildiz, “A molecular communication system model for particulate drug delivery systems,” *IEEE Trans. Biomed. Eng.*, vol. 60, pp. 3468–3483, Dec. 2013.
- [7] Y. Chahibi and I. F. Akyildiz, “Molecular communication noise and capacity analysis for particulate drug delivery systems,” *IEEE Trans. Commun.*, vol. 62, no. 11, pp. 3891–3903, Nov. 2014.
- [8] Y. Chahibi *et al.*, “Pharmacokinetic modeling and biodistribution estimation through the molecular communication paradigm,” *IEEE Trans. Biomed. Eng.*, vol. 62, no. 10, pp. 2410–2420, Oct. 2015.
- [9] A. Tjabben *et al.*, “Multipath signal prediction for in-body nanocommunication with volatile particles,” *Proc. 29th Eur. Wirel. Conf.*, pp. 41–46, 2024.
- [10] K. V. Srinivas, A. W. Eckford, and R. S. Adve, “Molecular communication in fluid media: The additive inverse gaussian noise channel,” *IEEE Trans. Inf. Theory*, vol. 58, no. 7, pp. 4678–4692, Jul. 2012.
- [11] P. I. Aaronson, J. P. T. Ward, and M. J. Connolly, *The Cardiovascular System at a Glance*. Wiley & Sons, Incorporated, John, 2012.
- [12] R. Aris, “On the dispersion of a solute in a fluid flowing through a tube,” *Proc. R. Soc. (London) A*, vol. 235, pp. 67–77, Apr. 1956.
- [13] F. Vakilipoor *et al.*, “The CAM model: An in vivo testbed for molecular communication systems,” *IEEE Trans. Mol. Biol. Multi-Scale Commun.*, pp. 1–1, 2025.